

only currents of Sn atoms around the edge of the island, then $\mu(R)$ would drop rapidly with island size, proportional to $1/R^3$ (17), and give a $v(R)$ that would increase with decreasing radius as $1/\sqrt{R}$. Thus, as long as D_d is nonzero, diffusion through the islands for sufficiently large R values should provide the dominant contribution to their mobility, consistent with our observations.

We can experimentally adjust the speed of the islands over several orders of magnitude by changing the temperature slightly around room temperature. In an Arrhenius plot of the velocity (Fig. 5B), the linearity suggests that the processes responsible for the island motion are activated with an energy of 900 meV. From the above analysis, this should be half of the activation energy associated with the product $D_d \rho_d \beta$. Because diffusion barriers, defect formation energies, and exchange energies are typically on the order of hundreds of meV, the activation energy we measure is reasonable within this model. From our measurements at 270 K, we find that the Sn-Cu exchange rate is roughly one atom per 4000 s. Assuming a value of ϵ on the order of 100 meV, typical diffusion prefactors on the order of 10^{12} s^{-1} , and the experimentally measured activation energy, we find that $(D_d \rho_d \omega^2 \epsilon \beta / k_B T)^{1/2}$ yields island velocities of the observed order of magnitude. So the simple picture of Fig. 4 seems to be consistent with everything we know at present about this system. Given the simplicity of the driving force for the motion of the reactive Sn islands, this mechanism of surface alloying might be expected to be common when surface diffusion is faster than exchange into the substrate.

We make three comments about the surface bronze formation: (i) The trajectories shown in Figs. 1 and 2 do not convey the full animation of the Sn island motion (9); the Sn islands often appear to react to their surroundings in a complex way (pausing when their best path is not obvious, for example) and are efficient in finding new unalloyed regions. It is interesting that such complexity can arise from such a seemingly simple situation as surface alloying. (ii) Surface free energy-driven motion of particles on liquid surfaces (or liquids on solid surfaces) is a familiar phenomenon (18–24); the observation of the similar motion of camphor particles across water dates to 1686 (23, 24) and was the subject of much discussion in the 19th century. It allowed Lord Rayleigh to estimate molecular dimensions and motivated him to perform an accurate determination of the surface tension of water (25), for example, and now reappears in the context of solids on the nanoscale. (iii) Control of the island motion presents the possibility of manipulation of surface alloy formation to create useful and novel nanoscale structures.

References and Notes

1. L. P. Nielsen *et al.*, *Phys. Rev. Lett.* **71**, 754 (1993).
2. A. Christensen *et al.*, *Phys. Rev. B* **56**, 5822 (1997).
3. F. Besenbacher *et al.*, *Science* **279**, 1913 (1998).
4. S. S. P. Parkin, *Annu. Rev. Mat. Sci.* **25**, 357 (1995).
5. See, for instance, A. K. Schmid, J. C. Hamilton, N. C. Bartelt, R. Q. Hwang, *Phys. Rev. Lett.* **77**, 2977 (1996).
6. E. Bauer, *Rep. Prog. Phys.* **57**, 895 (1994).
7. J. Erlewein, S. Hofmann, *Surf. Sci.* **68**, 71 (1977).
8. G. Contini, V. Di Castro, N. Motta, A. Scarlata, *Surf. Sci.* **405**, L509 (1998).
9. For movies of the motion of the islands in Figs. 1 and 2, see Science Online (www.sciencemag.org/cgi/content/full/290/5496/1561/DC1).
10. For convenience, our Cu crystals were grown as films on a Ru substrate. The films were more than 20 atomic layers thick, and the spacing between surface atomic steps was often several micrometers. Precise x-ray crystallography measurements show that the lattice spacing of these crystals is indistinguishable from that of bulk Cu [H. Zajonz, D. Gibbs, A. P. Baddorf, V. Jahns, D. M. Zehner, *Surf. Sci.* **447**, L141 (2000)].
11. Evidence for Sn-Cu exchange within islands rather than at island edges comes from experiments in which we completely covered the surface with the (2×2) Sn phase. Despite the absence of island edges, the rate of creation of the $(\sqrt{3} \times \sqrt{3})R30^\circ$ alloy phase was identical to the observed rate for islands.
12. N. C. Bartelt, in preparation.
13. J. M. Wen, S. L. Chang, J. W. Burnett, J. W. Evans, P. A. Thiel, *Phys. Rev. Lett.* **73**, 2591 (1994).
14. K. Morgenstern, G. Rosenfeld, B. Poelsema, G. Comsa, *Phys. Rev. Lett.* **74**, 2058 (1995).
15. S. C. Wang, G. Ehrlich, *Phys. Rev. Lett.* **79**, 4234 (1997).
16. W. W. Pai, A. K. Swan, Z. Y. Zhang, J. F. Wendelken, *Phys. Rev. Lett.* **79**, 3210 (1997).
17. S. V. Khare, N. C. Bartelt, T. L. Einstein, *Phys. Rev. Lett.* **75**, 2148 (1995).
18. F. D. Dos Santos, T. Ondarcuhu, *Phys. Rev. Lett.* **75**, 2972 (1995).
19. C. D. Bain, G. D. Burnett-Hall, R. R. Montgomerie, *Nature* **372**, 414 (1994).
20. M. K. Chaudhury, G. M. Whitesides, *Science* **256**, 1539 (1992).
21. F. Brochard, *Langmuir* **5**, 432 (1989).
22. P. G. de Gennes, *Physics A* **249**, 196 (1998).
23. L. E. Scriven, C. V. Sternling, *Nature* **187**, 186 (1960).
24. A. W. Adamson, *Physical Chemistry of Surfaces* (Wiley, New York, ed. 4, 1982), pp. 97–116.
25. Lord Rayleigh, *Philos. Mag.* **30**, 386 (1890).
26. Supported by the Office of Basic Energy Sciences, Division of Materials Sciences, U.S. Department of Energy, under contract DE-AC04-94AL85000.

10 July 2000; accepted 26 September 2000

High Shear Strain of Olivine Aggregates: Rheological and Seismic Consequences

M. Bystricky,* K. Kunze, L. Burlini, J.-P. Burg

High-pressure and high-temperature torsion experiments on olivine aggregates in dislocation creep show about 15 to 20% strain weakening before steady-state behavior, characterized by subgrain-rotation recrystallization and a strong lattice preferred orientation. Such weakening may provide a way to focus flow in the upper mantle without a change in deformation mechanism. Flow laws derived from low strain data may not be appropriate for use in modeling high strain regions. In such areas, seismic wave propagation will be anisotropic with an axis of approximate rotational symmetry about the shear direction. In contrast to current thinking, the anisotropy will not indicate the orientation of the shear plane in highly strained, recrystallized olivine-rich rocks.

Seismic anisotropy in oceanic and continental lithospheres is commonly attributed to deformation-induced lattice preferred orientations (LPOs) of olivine and pyroxene (1–6) and is used to determine flow patterns in the upper mantle (7, 8). To give weight to this interpretation, we must understand how olivine LPOs develop and evolve with strain in particular deformation settings. Flow in the mantle involves high strain and non-coaxial deformation, but most experimental studies on polycrystalline olivine have been performed under uniaxial compression, in which deformation is coaxial and the total amount of strain (equivalent strains <0.5) is limited (9–12). Olivine samples deformed to shear strains up

to 1.5 using a diagonal-cut assembly (13, 14) yielded useful microstructural and textural observations. However, these experiments may not have produced steady-state deformation textures. In addition, such an experimental arrangement does not allow a detailed rheological study, because combined compressional and simple shear components contribute to the deformation and because the state of stress is poorly known at high strains (15). Here we present results on the experimental deformation of olivine aggregates in torsion yielding bulk shear strains up to $\gamma = 5$. The aim of this study was to achieve non-coaxial deformation and to investigate the detailed microstructural, textural, and rheological evolution of polycrystalline olivine over a larger strain range than previously accessible.

Olivine aggregates were hot-pressed from San Carlos olivine powders (16). Deformation experiments were carried out in a high-

Geologisches Institut, ETH-Zentrum, 8092 Zürich, Switzerland.

*To whom correspondence should be addressed. E-mail: misha@erdw.ethz.ch

REPORTS

pressure and high-temperature torsion apparatus (17), in which any small element of the sample undergoes deformation at constant strain rate by simple shear (18). The shear stress and shear strain rate at the outer surface of the cylindrical sample were derived from the measured torque and twist rate, respectively (19). The experiments were performed at 1200°C and 300 MPa confining pressure, with the oxygen fugacity near the Fe/FeO buffer (10^{-12} bars). Fourier transform infrared (FTIR) spectroscopy analyses of deformed samples indicated that they contained less than 30 molar parts per million (ppm) H/Si (20). Samples were deformed to different amounts of bulk shear strain, under two constant angular displacement rates corresponding to constant shear strain rates of either $6 \times 10^{-5} \text{ s}^{-1}$ or $1.2 \times 10^{-4} \text{ s}^{-1}$ at the outer surface of the sample. For both deformation series, a peak stress occurred at a shear strain $\gamma \sim 0.1$, followed by 15% weakening up to $\gamma \sim 0.5$ (Fig. 1). At higher strains, the flow stress was nearly steady-state, leading to a total weakening of the aggregate of about 20% from the peak stress to the flow stress at $\gamma \sim 5$. Stress exponents of $n = 3.3$ determined after the weakening suggest dislocation creep as the rate-limiting mechanism, even at high strains.

Microstructures were analyzed with optical and electron microscopy. Thin sections were cut perpendicular to the cylinder radius and within 200 to 300 μm of the sample outer edge. In such planes, deformation is nearly simple shear (18). With increasing strain, the average grain size reduced by dynamic recrystallization (Fig. 2). At shear strains $\gamma \sim 0.5$, a typical deformation microstructure displays evidence of incipient recrystallization (Fig. 2, C and D). At $\gamma \sim 2$, core-and-mantle structures suggest recrystallization by subgrain rotation (Fig. 2, E and F). The matrix wraps around porphyroclasts and resembles the mosaic texture described in natural peridotites (21). With further strain, the porphyroclasts become more elongated, with an oblique shape fabric consistent with the sense and amount of shear. At $\gamma \sim 5$, recrystallization is nearly complete and a fluidal mosaic microstructure (21) with a strong foliation sub-parallel to the shear plane has developed (Fig. 2, G and H). The $\sim 5\%$ of remaining porphyroclasts consist of ribbons with highly stretched tails (blue grains) and asymmetric porphyroclasts showing subgrains and deformation features (white grains). High-resolution orientation imaging maps are consistent with the observed microstructures (Fig. 3). The spatial distribution of small-angle misorientations within the clasts confirms the formation of subgrains with a size similar to the recrystallized grains, providing further evidence for recrystallization by subgrain rotation.

LPOs were measured using electron back-

scatter diffraction (EBSD). During deformation, the texture evolved through a transient deformation texture ($\gamma \sim 0.5$) into a recrystallization texture at high strain (Fig. 4). At $\gamma \sim 0.5$, the [010] crystallographic axes tend to align normal to the shear plane and the

[100] axes develop two maxima, one parallel to the shear direction and one oblique to the shear direction. This LPO fits with previous low strain experimental results (13, 14) and with numerical simulations (22, 23). At higher strains, the texture is much stronger and

Fig. 1. Shear stress versus shear strain for samples deformed at 1200°C and 300 MPa at constant nominal shear strain rates of $6 \times 10^{-5} \text{ s}^{-1}$ (gray curve) and $1.2 \times 10^{-4} \text{ s}^{-1}$ (black curve). Conversion from torque and twist of torsion deformation into shear stress and strain was performed as in (19). The peak stresses agree well with dislocation creep flow laws for olivine aggregates determined in axial compression experiments (12). Stepping tests performed at high strains yielded stress exponents n ($n = 3.2$ at $\gamma \sim 1.2$ and $n = 3.3$ at $\gamma \sim 3.2$) typical of deformation by dislocation creep. Shaded area (left) shows magnified view of the low strain interval at right ($\gamma \leq 0.2$), up to equivalent strains ($\sim 10\%$) where rheological data are typically obtained in compression experiments. At these low strains, deformation often appears to be steady-state because the onset of weakening is rarely reached.

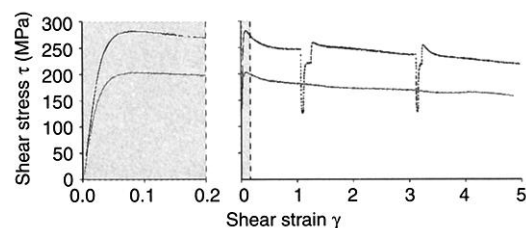
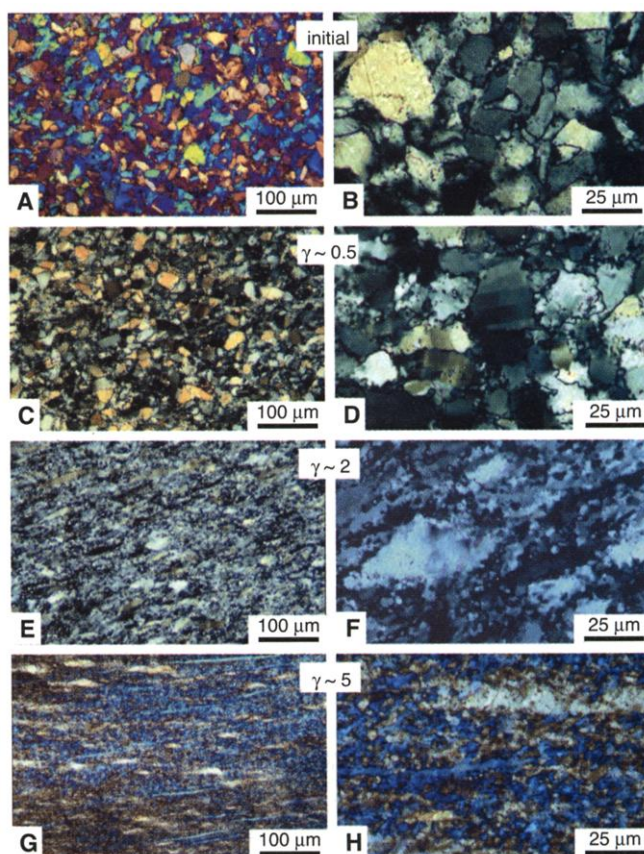


Fig. 2. Optical micrographs in cross-polarized light [from thin sections cut as in (18)] of olivine aggregates deformed at $6 \times 10^{-5} \text{ s}^{-1}$ to different shear strains. Shear sense is dextral. (A and B) Starting material. Olivine aggregate hot-pressed for 12 hours, showing an equigranular fabric with an average grain size of 20 μm . Most grains have euhedral shapes with low aspect ratios. Grain boundaries are straight to curved. Few deformation features such as lamellae and subgrains are visible within the grains. The micrograph in (A) was taken using a gypsum plate. (C and D) Deformed protolith. Deformation microstructure at shear strain $\gamma \sim 0.5$. Evidence of dislocation creep and recovery in the form of deformation lamellae and 3 to 4 μm subgrains. Grain boundaries are curved to lobate, with bulges indicating the onset of recrystallization. A weak oblique shape preferred orientation is consistent with the sense of shear. (E and F) Protomylonite. Partially recrystallized microstructure at $\gamma \sim 2$. Recrystallized grain size is 3 to 4 μm . Elongated porphyroclasts with deformation lamellae have aspect ratios R from 2 to 6 ($R = 5.8$ for the finite strain ellipse at $\gamma = 2$). Core-and-mantle structures and a subgrain size similar to the recrystallized grain size provide evidence for recrystallization by subgrain rotation. (G and H) Ultramylonite. Fluidal mosaic microstructure at $\gamma \sim 5$. The recrystallized matrix ($\sim 95\%$ volume) is very homogeneous with $\sim 3 \mu\text{m}$ equant grains. Two types of porphyroclasts with distinct crystallographic orientations remain. Highly elongated ribbon grains (blue) are in an orientation for easy slip on (010)[100] and track the bulk strain. Their aspect ratios ($R = 25$ to 40) are consistent with the finite strain ellipse at $\gamma = 5$ ($R = 27$). A second type of porphyroclasts (white) with lower aspect ratios ($R < 10$) are full of subgrains and deformation features, are strongly asymmetric in shape, and have an oblique lattice orientation. Both types have average grain areas equal to those of the starting grains (equivalent diameter, $\sim 20 \mu\text{m}$), suggesting that their shapes are due entirely to strain without major coalescence.



more symmetric with respect to the shear kinematics. It has a sharp [100] maximum oriented parallel to the shear direction and girdles of [010] and [001] normal to that direction. Individual measurements of 50 ribbon porphyroclasts indicate that nearly all have a single preferred orientation, consistent with “easy slip” on the (010)[100] system. For the asymmetric porphyroclasts, the [100] axes are distributed oblique to the shear direction, as in the low strain deformation texture. The observed high strain texture differs from numerical simulations with or without modeling recrystallization (22, 23) by the [010] and [001] girdle normal to the shear

direction rather than a [010] point maximum perpendicular to the shear plane.

An important goal in studying mantle dynamics is to determine the flow direction and shear plane from seismic observations. Seismic properties of deformed samples (compressional wave velocity V_p , shear wave splitting dVs , and polarization of fast shear wave $Vs1$ pol) were calculated from the measured LPO (Fig. 4). The data for high shear strains suggest that a large V_p anisotropy (here half of the single crystal anisotropy) can develop in highly sheared parts of the mantle. The V_p maximum and dVs minimum are parallel to the shear direction, along with an

approximate axial symmetry in all the velocity distributions about that direction. As V_p is minimum anywhere along a girdle normal to the shear direction, it does not indicate the orientation of the shear plane, by contrast to previous conclusions based on experiments conducted to lower strains (13, 14). These results imply that seismic investigations of the mantle (e.g., V_p and V_s deep seismic sounding, near vertical reflection, and teleseismic shear wave splitting) may indicate the flow direction, but will not identify the shear plane in highly recrystallized olivine mylonites.

Experimental deformation to high shear strain of olivine aggregates produces a stable LPO and recrystallized microstructure consistent with observations in highly deformed natural peridotites (21, 24). Although sample size, grain size, temperature, and strain rate conditions may be different in the laboratory than in nature, the correspondence in microstructures provides confidence that it is possible to scale results obtained in experiments to natural conditions. In addition, the 15 to 20% observed weakening may provide a way to focus flow in the upper mantle without the need to invoke a change in deformation mechanism (25). In subduction zones, high shear strains may lead to strain localization where hot mantle convects past the upper side of cold slabs. In regions of extensional deformation, strain weakening may focus on major detachment zones near the crust-mantle boundary, for example during the development of passive margins (26, 27). Seismic discontinuities recently identified in the upper mantle (28, 29) may correspond to such shear zones. For these regions of localized shear strain, the application of rheologies derived from low strain data would be inappropriate.

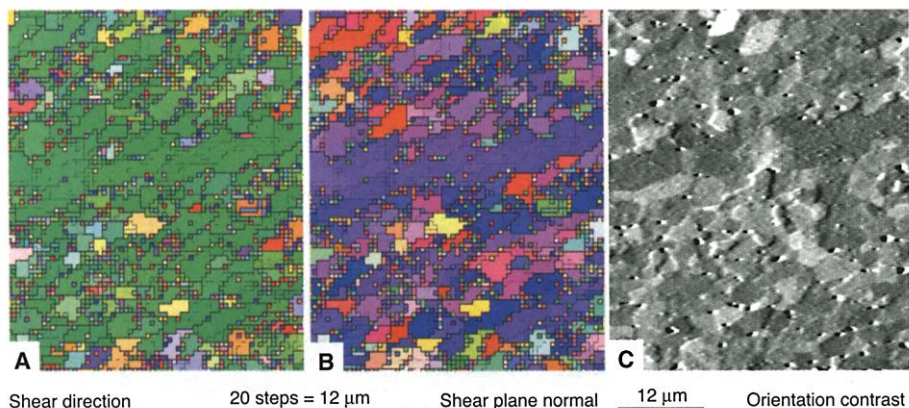
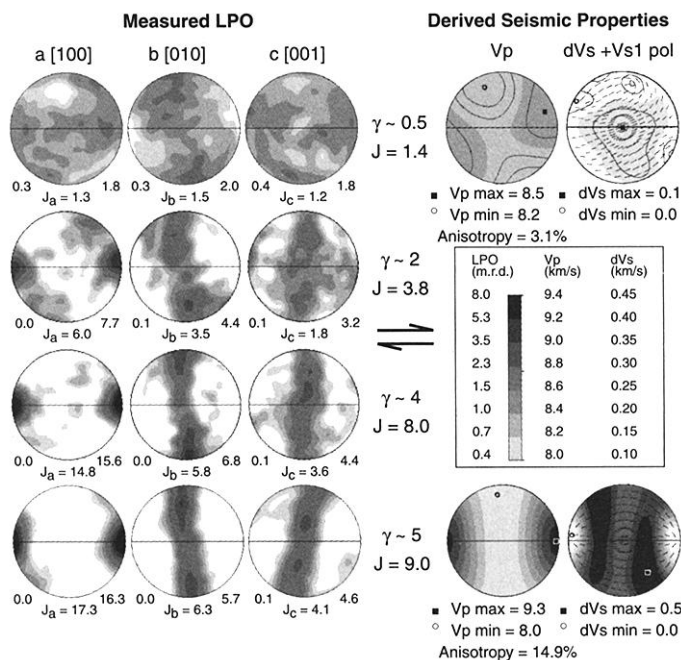


Fig. 3. Microstructure of olivine aggregate deformed to $\gamma \sim 5$ showing ribbon grains within recrystallized matrix. (A and B) High-resolution orientation imaging maps with color key according to inverse pole figures of shear direction and shear plane normal, respectively. Thick lines between pixels indicate grain boundaries (nearest neighbor misorientation angle $\omega > 15^\circ$) and thin lines mark subgrain boundaries ($2^\circ < \omega < 15^\circ$). Recrystallized grains in the matrix have sizes of about 3 to 6 μm and have various orientations with [100] preferably toward the shear direction. A highly elongated ribbon shows similarly sized subgrains and is in approximate orientation (031)[100]. (C) Scanning electron microscope orientation contrast image at same magnification of a different region with similar features.

Fig. 4. Pole figures and seismic properties of olivine aggregates deformed in dextral shear. All figures are upper hemisphere equal area projections. Pole figures are scaled in multiples of random distribution (m.r.d). Texture indices are indicated for the overall textures (J) and each pole figure separately (J_a, J_b, J_c). Minima and maxima are indicated to the left and right of measured pole figures, respectively. Seismic properties were derived from the LPO data using the Voigt volume averaging scheme [programs from (32, 33)].



References and Notes

- H. H. Hess, *Nature* **203**, 629 (1964).
- N. I. Christensen, *Geophys. J. R. Astron. Soc.* **76**, 89 (1984).
- A. Nicolas, N. I. Christensen, in *Composition, Structure and Dynamics of the Lithosphere-Asthenosphere System*, K. Fuchs, C. Froidevaux, Eds. (American Geophysical Union, Washington, DC, 1987), vol. 16, pp. 111-123.
- V. Babuska, M. Cara, *Seismic Anisotropy in the Earth* (Kluwer, Dordrecht, 1991).
- D. Mainprice, P. G. Silver, *Phys. Earth Planet. Inter.* **78**, 257 (1993).
- W. Ben Ismail, D. Mainprice, *Tectonophysics* **296**, 145 (1998).
- M. K. Savage, *Rev. Geophys.* **37**, 65 (1999).
- K. M. Fischer, E. M. Parmentier, A. R. Stine, E. R. Wolf, *J. Geophys. Res.* **105**, 16181 (2000).
- H. G. Avé Lallemant, N. L. Carter, *Geol. Soc. Am. Bull.* **81**, 2203 (1970).
- P. N. Chopra, M. S. Paterson, in *The Effect of Deformation on Rocks*, G. S. Lister, H. J. Behr, K. Weber, J. J. Zwart, Eds. (Elsevier, Amsterdam, Netherlands, 1981), vol. 78, pp. 453-473.
- P. N. Chopra, M. S. Paterson, *J. Geophys. Res.* **89**, 7861 (1984).
- S. I. Karato, M. S. Paterson, J. D. FitzGerald, *J. Geophys. Res.* **91**, 8151 (1986).
- S. Q. Zhang, S. Karato, *Nature* **375**, 774 (1995).
- _____, J. FitzGerald, U. H. Faul, Y. Zhou, *Tectonophysics* **316**, 133 (2000).

15. T. E. Tullis, J. Tullis, in *Mineral and Rock Deformation; Laboratory Studies; The Paterson Volume*, B. E. Hobbs, H. C. Heard, Eds. (American Geophysical Union, Washington, DC, 1986), vol. 36, pp. 297–324.
16. Samples were prepared as follows: Optically transparent single crystals of San Carlos olivine ($Mg_{0.906}Fe_{0.091}Ni_{0.003}SiO_4$) were crushed with a tempered steel piston and were ground using an agate pestle and mortar. The material was dry-sieved, resulting in powders with 15- to 32- μ m grain sizes. Samples were cold-pressed in an iron jacket under uniaxial stress (~ 150 MPa). Powders and cold presses were stored at 150°C in a 1-bar oven. Cold-pressed samples were isostatically hot-pressed in an internally heated gas medium vessel at 1200°C and 300MPa confining pressure for 12 hours, and were immediately deformed.
17. M. S. Paterson, D. L. Olgaard, *J. Struct. Geol.* **22**, 1341 (2000).
18. Web figure 1 illustrating the sample assembly is available at *Science Online* at www.sciencemag.org/cgi/content/full/290/5496/1564/DC1.
19. Rheological parameters in torsion experiments were obtained as follows: Shear strain γ at a given position in the sample is proportional to twist angle θ and radial distance from cylinder axis. The same holds true for rates $\dot{\gamma}$ and $\dot{\theta}$. Most of the applied torque M is supported by the outer rim of the specimen. For a homogeneous isotropic material, the shear stress τ is proportional to M , assuming a uniform power law rheology $\dot{\gamma} \propto \tau^n$ with a constant stress exponent n throughout the sample. A related power law $\dot{\theta} \propto M^n$ holds with the same exponent n (17, 30, 31). Stepping tests (where M is measured as a function of $\dot{\theta}$) allow n to be determined at different total shear strains γ .
20. Infrared spectra were measured by S. Mackwell at the Bayerisches Geoinstitut, Universität Bayreuth.
21. A. M. Boullier, A. Nicolas, *Phys. Chem. Earth* **9**, 467 (1975).
22. A. Tommasi, B. Tikoff, A. Vauchez, *Earth Planet. Sci. Lett.* **168**, 173 (1999).
23. H. R. Wenk, C. N. Tomé, *J. Geophys. Res.* **104**, 25513 (1999).
24. A. Nicolas, *Rev. Geophys.* **24**, 875 (1986).
25. S. Karato, P. Wu, *Science* **260**, 771 (1993).
26. B. Wernicke, B. C. Burchfiel, *J. Struct. Geol.* **4**(2), 105 (1982).
27. G. Boillot, G. Feraud, M. Recq, J. Girardeau, *Nature* **341**, 523 (1989).
28. F. A. Cook, A. J. van der Velden, K. W. Hall, B. J. Roberts, *Geology* **26**, 839 (1998).
29. ———, *Tectonics* **18**, 1 (1999).
30. G. R. Canova, S. Shrivastava, J. J. Jonas, C. G'Sell, in *Symposium on Formability of Metallic Materials—2000 A.D.*, J. R. Newby, B. A. Niemeier, Eds., Chicago, IL, 24 to 25 June 1980 (American Society for Testing and Materials special publication 753, Chicago, 1982), pp. 189–210.
31. J. A. Bailey, in *Metals Handbook, Vol. 8 Mechanical Testing* (American Society for Metals, Metals Park, OH, 1985), pp. 139–144.
32. H. R. Wenk, S. Matthies, J. Donovan, D. Chateigner, *J. App. Cryst.* **31**, 262 (1998).
33. D. Mainprice, *Comput. Geosci.* **16**, 385 (1990).
34. We thank M. Paterson for the design and installation of the torsion apparatus, S. Mackwell for FTIR measurements and for stimulating discussions, M. Schmocker and A. Barnhoorn for assistance, R. Hofmann for workshop support, R. Wessicken for SEM maintenance, and F. Pirovino for thin section preparations. We also gratefully acknowledge two anonymous referees for providing constructive reviews. Supported by the Swiss Nationalfond No. 2000-052494.97/1.

18 July 2000; accepted 10 October 2000

Quantitative Imaging of Lateral ErbB1 Receptor Signal Propagation in the Plasma Membrane

Peter J. Verveer,^{1*} Fred S. Wouters,^{1*} Andrew R. Reynolds,^{2*} Philippe I. H. Bastiaens^{1,2†}

Evidence for a new signaling mechanism consisting of ligand-independent lateral propagation of receptor activation in the plasma membrane is presented. We visualized the phosphorylation of green fluorescent protein (GFP)-tagged ErbB1 (ErbB1-GFP) receptors in cells focally stimulated with epidermal growth factor (EGF) covalently attached to beads. This was achieved by quantitative imaging of protein reaction states in cells by fluorescence resonance energy transfer (FRET) with global analysis of fluorescence lifetime imaging microscopy (FLIM) data. The rapid and extensive propagation of receptor phosphorylation over the entire cell after focal stimulation demonstrates a signaling wave at the plasma membrane resulting in full activation of all receptors.

Ligand-driven ErbB1 activation is generally thought to occur through the formation of stable receptor dimers (1–5). The proximity of the two ErbB1 receptors in the stable dimer allows subsequent transactivation by cross-phosphorylation of target tyrosine residues by the receptor tyrosine kinase domain, both located in the cytoplasmic tail of the receptor (6, 7). Signal transduction then proceeds through recruitment to the receptors of phosphotyrosine-binding adaptor and effector

proteins, such as Grb2, SHC, and p85 (8–10). We provide evidence for a different ErbB1 signaling mechanism of ligand-independent lateral propagation of receptor activation in the plasma membrane where the activated receptor dimer is a transient rather than a stable feature. To show this, we induced local activation of ErbB1-GFP by applying EGF covalently attached to beads (EGF-beads) and monitored the phosphorylation state of the receptors across the whole cell. The extent of ErbB1 receptor phosphorylation was mapped by measuring FRET between ErbB1-GFP and a Cy3-labeled antibody to phosphotyrosine (Cy3/PY72).

The occurrence of FRET causes the fluorescence lifetime of the phosphorylated receptor to decrease (11–13), which is detected using FLIM (14–17). Efficient FRET will

occur only when the Cy3 acceptor is brought within nanometer range of the GFP donor by binding of the antibody to the phosphorylated receptor (11). A global FLIM analysis technique was developed (18) that uses the understanding that the receptor exists in two states, phosphorylated or unphosphorylated, each with a unique associated fluorescence lifetime (Fig. 1A). As a result, quantitative maps of the populations of each state are obtained (Fig. 1B). In addition, the lifetime of each state is determined, from which the true FRET efficiency in the receptor-antibody complex can be calculated. This approach allows quantitative and precise mapping of the relative concentration of phosphorylated protein in cells, whereas earlier approaches were qualitative (12, 19).

To study the lateral propagation of ErbB1-GFP phosphorylation, the population distribution of phosphorylated receptors in cells after focal stimulation with 0.8- μ m diameter EGF-beads (20, 21) was compared with the distribution after exposure to a saturating dose (0.1 μ g/ml) of soluble EGF. Groups of MCF7 cells expressing ErbB1-GFP were microinjected with Cy3-labeled Fab fragments (22) of a phosphotyrosine-specific antibody (Cy3/FabPY72) and stimulated. Average ErbB1-GFP expression levels in MCF7 cells (5×10^5) were half that of A431 cells, as judged by the fluorescence intensity of receptor-bound Cy3-EGF. Cells treated with soluble EGF showed a homogeneous phosphorylation pattern at the plasma membrane that was maximal 15 min after stimulation (Fig. 2A). Cells stimulated with EGF-beads (red dots, Fig. 2A) also exhibited an extended phosphorylation pattern, to the same extent as found after stimulation with soluble EGF, indicative of extensive lateral spreading of ErbB1 phosphorylation.

In these experiments, the kinetics of anti-

¹Cell Biology and Cell Biophysics Program, European Molecular Biology Laboratory, Meyerhofstrasse 1, 69117 Heidelberg, Germany. ²Cell Biophysics Laboratory, Imperial Cancer Research Fund, 44 Lincoln's Inn Fields, London, WC2A 3PX, UK.

*These authors contributed equally to this work. †To whom correspondence should be addressed. E-mail: philippe.bastiaens@embl-heidelberg.de